Chapter 06

Microstructure-based creep strain modeling of steel 316LN at 140-275 MPa / 600-650 ºC

Abstract: In this work, microstructural variables reliant creep model was used to simulate the creep curves of steel 316LN. Model variables include densities of mobile and forest dislocations and average dislocation glide distance. The model assimilated, hardening, recovery, precipitate growth and cavitation damage to address the creep behaviour. As an output, model is capable to deliver the creep strain as well as the evolution of each microstructure dependent variables. Theoretical creep curves are compared with the experimental creep data and reasonable agreement was obtained. The model predicts the important parameters that affect the creep behaviour and at the end of simulations, densities of mobile and forest dislocations, average dislocation glide distance, internal stress, effective stress, dislocation velocity and mobility lie in the range of 7.74 $\times 10^{12}$ - 11.58 $\times 10^{12}$ m^{-2} and 2.27 $\times 10^{13}$ - 3.96 $\times 10^{13}$ m^{-2}, 9.01-9.50 μm, 68.48-92.02 MPa, 57.06-164.92 MPa, 2.37 $\times 10^{-12}$ - 1.45 $\times 10^{-11}$ m/s and 1.61 $\times 10^{-10}$ - 3.41 $\times 10^{-10}$ $mPa^{-1}s^{-1}$ for the explored conditions. Furthermore, the evolution of aforementioned parameters with ongoing creep is discussed meticulously. It can be deduced that the synergistic effect of an increase in dislocation density leading to pile-ups, coarsening of precipitates, and cavitation leads to failure of this steel. discussed thoroughly.

6.1. Introduction

316 LN austenitic stainless steel is an important class of structural material and a potential candidate for power plant components. It possesses reasonably good elevated temperature

mechanical properties, resistance against stress induced corrosion, sufficient weldability and it is compatible with sodium coolant [21, 22, 239-242]. The structural parts made of this steel and exposed to stresses at elevated temperature are prone to creep failure. Thus, it's very important to obtain the understanding about the underlying deformation and failure mechanisms, so that safe life can be estimated to avoid any accident [243]. In that direction, out of several possibilities, physical-based models can be an important tool, as they are capable to address the deformation behaviour as well as the subsequent substructure evolution in detail. Considering the constant strain rate deformation and invoking the effect of globularization on flow softening and stress relaxation, Babu et al. [63] proposed a theoretical framework that addressed the deformation behaviour and subsequent substructure evolution of Ti-6Al-4V. Similar approach was used by Lindgren et al. [34] to model the deformation and corresponding microstructure evolution in AISI 316. Herein, the strengthening contributions from mobile and immobile configurations of dislocations, dislocation cell and Hall-Petch effect were considered. Furthermore, Fisk et al. [3] set up a physical based model to investigate the deformation characteristics of Inconel 718. Lin et al. [64] developed an unified dislocations reliant approach to explore the deformation behaviour of superalloy by invoking the concepts of work hardening, glide recovery and dynamic recrystallization. Li et al. [36] proposed set up of constitutive equations to elucidate the deformation behaviour in the near- α titanium alloy by taking the strengthening contributions from immobile dislocations and Hall-Petch effect. In the similar way, physical based frameworks were also proposed to address the creep characteristics of different materials. A composite model was proposed by Barkar et al. [155] for 9-12 % Cr steels with the assumption of equal strain accumulation in substructure boundaries and its interior regime. The internal variable considered for this model were subgrain size, free dislocation density and width of substructure boundaries.

Furthermore, considering an additional internal variable, that is immobile dislocation density, Magnusson et al. [49] proposed a set of equations to achieve theoretical creep strain for tempered martensitic steels, for up to secondary stage. Zhu et al. [148] proposed the model to predict the creep strain of nickel based single crystal super alloys employing the dislocation density and precipitate contribution. In case of copper, Sui et al. [244] and for steel Praveen et al. [245] proposed a set of constitutive equations to study the transient and secondary creep regime.

Apart from these physical-based models, empirical and hybrid (combination of physical and empirical) models were also established to study the creep response. In case of empirical models, Norton's power law ($\dot{\varepsilon} = A\sigma^n$, where A and n are in conventional sense) equation is the basic one, that have been used for so many years [246]. Researchers have further explored and attempted to develop the phenomenological models more [17, 20, 199, 209, 211, 246-249] to capture the creep response of materials that are often used for structural components. Invoking the artificial intelligence approach, Baraldi et al. [247] set up a constitutive model, originating from Norton power law, to study the creep response of steel [246]. The model was also implemented to finite element codes and the simulations demonstrated the entire creep regimes. Kim et al. [20] employed Kachonov-Rabotnov type [209, 211] damage model to characterize the creep in 316 LN steel and deformation rate was shown to be dependent of stress, strain, temperature and damage parameters. Follansbee et al. [250] also developed the constitutive model for steel 316 LN and creep deformation behaviour was studied in light of varying nitrogen content and grain size. Praveen et al. [249] and Christopher et al. [199] explored the creep response of 316 LN steel employing the Kachonov-Rabotnov type [209, 211] approach. Esposito et al. [17] estimated the minimum creep rate of 316 H by incorporating the contribution from both the dislocation and diffusion creep. Basoalto et al. [248] proposed the creep rate equations for superalloys IN738LC by considering

the internal damage state variables such as normalised back stress, reference strain rate, damage contribution from dislocation and precipitate coarsening. With respect to the hybrid models, Basirat et al. [55] formulated a model for 9 % Cr steel, considering the multiple microstructure dependent variables such as density of mobile and dipole dislocations configurations and mean size of precipitates. At the same time, damage caused by precipitate coarsening, effect of solute depletion and cavitation damage were also considered by invoking the continuous damage mechanics (CDM) approach. Similarly, Surya et al. [57, 58] proposed a physical based creep model that considered additional microstructure variables that were subgrain size and boundary dislocation density. The model also used CDM concept to incorporate various damage mechanisms to simulate the most part of the creep strain curves.

The literature survey suggests that some of the models [20, 199, 247-249] have the ability to address the complete creep curves, but they have not demonstrated the physics behind the microstructural evolution. Similarly, if physical models [49, 155] have shown the evolution of few selective variables, they are not capable to model complete creep curves. It is rare to find out a model that simulate the large portion of creep curve and also demonstrates the variation of each variable with ongoing creep.

Thus, this work focuses on modelling the creep strain curves of 316 LN steel using a physical based approach that relies on density of mobile and forest dislocation configurations, and average dislocation glide spacing. The total measured strain was considered to be due to the dislocation motion and softening associated with coarsening of precipitates and cavitation. This work presents significant advancement compared to existing literature as,

i. A more generalized dislocation mobility model is assimilated that considers the temperature dependency.

ii. The concept of effective stress was considered in place of applied stress for estimating dislocation mobility and glide velocity.

4.2 The evolution of each variable such as, density of mobile and forest dislocation configurations, average dislocation spacing, internal stress, effective stress, velocity of dislocations, dislocation mobility, size of precipitates and damage parameters, is demonstrated and discussed thoroughly.

6.2. Material and input parameters

Steel 316 LN was used for this study and its composition (in wt.%) was Carbon 0.025, Chromium 17.570, Manganese 1.740, Molybdenum 2.530, Nitrogen 0.140, Nickel 12.150, Phosphorous 0.017, Sulphur 0.004, Silicon 0.200 and remaining iron. It was heated to 1100 ^{o}C and once soaked for 30 minutes, and then water quenched. Creep strain curves used for the modelling purpose were obtained by testing the cylindrical specimens with gauge diameter and length of 10 mm and 50 mm, respectively. Tensile creep testing machine were used with a constant load set-up to get the creep data at 140-275 MPa / 600-650 ^{o}C. LOM and TEM were used to characterize the microstructure. Initial inputs such as densities of mobile and forest dislocations, radius of $M_{23}C_6$ type carbides and radius of MX type carbonitride precipitates were taken from the previously published works (see Table 6.1). TEM micrograph of the as-received sample, shown in Figure. 6.1, reveals the presence of dislocation.

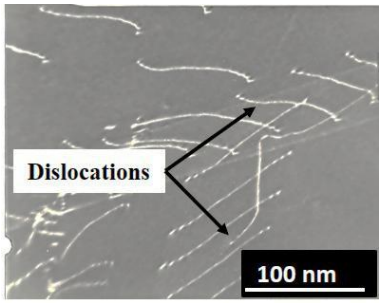

Figure 6.1.TEM micrograph of as received 316 LN stainless steel sample

Table 6.1. Initial input parameters used in the model

Parameters	Magnitude	References
Mobile ⊥ density	$6.50 \times 10^{12}\ m^{-2}$	[18]
Forest ⊥ density	$11.00 \times 10^{12}\ m^{-2}$	[18]
Average dislocation glide distance	1.00×10^{-5} m	[41]
Radius of $M_{23}C_6$ precipitates	15.00 nm	[251]
Radius of MX precipitates	19.00 nm	[251]

6.3. Creep model for steel 316 LN

6.3.1. Microstructure consideration and its evolution

There have been several attempts to address the plastic deformation employing microstructure based models. The variation of forest dislocation density with ongoing deformation was considered by Kocks-Mecking approaches [32, 252] in the framework of single internal variable physical model. At later stages mobile dislocation density was also introduced along with forest ones by Kubin et al. [253] to provide the improved description of deformation behaviour in the metallic materials. Furthermore, Barlat et al. [27] introduced a third internal variable, that was average travel path of dislocations, to provide a more accurate prediction of deformation response in a Al-alloy. The approach in [27] was also explored by Surya et al. [41] to assess its applicability for addressing the deformation response of steel 304HCu.

It was observed that, three internal variable approaches work well when it comes to address the deformation behaviour of austenitic steels. Thus, mobile dislocations, forest dislocations and average dislocation glide distance were considered to describe the microstructure and corresponding internal variables in this work. Further, as the $M_{23}C_6$ carbides and MX carbonitrides

type second phase particles play a vital role in creep strengthening, their evolution was also considered. Variation in mobile dislocation density during creep can be addressed by combining a productive term $(M/b\lambda_{ms})\,\dot{\varepsilon}$ and reduction term $(M/b\lambda_{mean})\,\dot{\varepsilon}$. The production term is associated with multiplication of the dislocations that occurs due to the active Frank-Read (F-R) sources and reduction term is related to annihilation caused by the dynamic recovery. Thus, under the creep loading condition, variation in mobile dislocation density (ρ_m) can be given as [27],

$$\frac{d\rho_m}{dt} = -M\left[\frac{1}{b\lambda mean} - \frac{1}{b\lambda_{ms}}\right]\dot{\varepsilon} \tag{6.1}$$

Similarly, the evolution of second internal variable, i.e., density of forest dislocations also consists of production and reduction terms, i.e., $(M/b\lambda_{mean})\,\dot{\varepsilon}$ and $(M\rho_f K_2)\,\dot{\varepsilon}$, respectively. Thus, the differential equation that describes the variation in the density of forest dislocations during creep can be given as [27],

$$\frac{d\rho_f}{dt} = M\left[\frac{1}{b\lambda mean} - K_2\rho_f\right]\dot{\varepsilon}, \tag{6.2}$$

where ρ_f represents the density of forest dislocations and K_2 is a parameter related to glide recovery. During the creep deformation of steel 316LN, dislocations move up to a certain distance and then they stop, due to encounter with other barriers (for example, dislocations with same sign on same glide plane). This distance is said to be average dislocation glide distance and its evolution can be addressed by a production term $(\lambda_{ms}K_{Lm}\dot{\varepsilon})$ and reduction term $(\lambda_{mean}K_{Lm})$. The rate of change of average dislocation glide distance can be given as [27],

$$\frac{dL_m}{dt} = -K_{Lm}[L_m - \lambda_{ms}]\dot{\varepsilon} \tag{6.3}$$

where, K_{Lm} is the rate at which average dislocation glide distance saturates. The derivation of Equations (6.1), (6.2) and (6.3) is based on the differential equations published in Barlat et al. [27]

and Surya et al. [41], where rate equations were developed with respect to strain, as the strain rate was constant. In case of creep, time is an important parameter, thus, the differential equations in [27, 41] were modified with respect to time to predict the creep strain.

6.3.2. Internal stress and effective stress

Microstructure offers resistance against any possible deformation and in the form of stress, this internal resistance is known as internal stress. In recent past, several ways have been explored to evaluate the internal stress. In this direction, Ghoniem et al. [47] and Salazar et al. [170] have proposed the equation for internal stress, comprised of the dipole dislocation density and the contributions from precipitates. Similarly, Barkar et al. [155] established an the equation based on the mobile dislocation density and the precipitates. As the stress fields of mobile and dipole dislocations are significant, by taking the contribution from both dislocations, Basirat et al. [55] and Surya et al. [57, 58] proposed the evolution law for the estimation of the internal stress. As the internal stress model developed in [57, 58] worked well for steels, this work also considers the similar approach where internal stress is expressed as,

$$\sigma_{int} = \alpha M G_T b \sqrt{\rho_m + c_f \rho_f} \ , \tag{6.4}$$

where c_f is a weight factor for forest dislocation. The weight factor is important, as it unify the contributions from both, mobile and forest dislocations, under a single α value. As a consequence of the internal stress the total amount of the applied stress is not available for dislocation movement and creep deformation. Some part of total stress is always exhausted to overcome the microstructural resistance/internal stress. Thus, an effective stress that is the remaining amount of applied stress is only available for plastic deformation and it is assimilated in the model with the following expression [57, 58],

$$\sigma_{effe} = \sigma_{appl} - \sigma_{int}\,, \tag{6.5}$$

6.3.3. Dislocation velocity and dislocation mobility

Materials under creep loading conditions tend to deform plastically due to movement of dislocations (in case of dislocation creep). Depending on loading conditions, the movement of dislocations can be glide, climb or both. In the literature, several efforts have been employed to compute the dislocation velocity. In [109, 254] dislocation velocity is comprised of the dislocation mobility M_c, Burgers vector and the applied stress through the following expression,

$$v_{gl} = M_c b \sigma_{appl}. \tag{6.6}$$

This model is good enough to predict the velocity, if the dislocation movement is only due to climb mechanism. The model underestimates the dislocation velocity, if glide mechanism is dominant, as in case dislocation creep. As discussed earlier, all the applied stress is not available for creep thus in Equation (6.6), applied stress needs to be replaced by effective stress. Another aspect is, as the dislocations move on the slip planes and intersects, they form jogs. The jogs are not able to move in the slip plane and climbing helps to move them further [109]. Based on the above discussion, herein, the dislocation velocity that consists of a contribution from glide and climb both, as well as modified in terms of effective stress, can be represented by the following expression,

$$v_{cg} = M_{cg} b \sigma_{eff}\,, \tag{6.7}$$

where, v_{cg} is climb-glide velocity and M_{cg} is the mobility driven by both glide and climb process. The conventional, combined glide-climb dislocation mobility can be expressed as [254, 255],

$$M_{cg} = \frac{D_0 b}{k_B T}\, e^{\frac{\sigma_{appl} b^3}{k_B T}} e^{-\frac{Q}{RT}\left[1-\left(\frac{\sigma_{appl}}{\sigma_{max}}\right)^2\right]}, \tag{6.8}$$

where, $\sigma_{max} = 1.5 \times \sigma_{UTS}$, and Q being the activation energy for self-diffusion. The limitation of Equation (6.8) in [255] is, as it used temperature independent UTS and assumed that the whole applied stress is available for dislocation movement. In order to make the Equation (6.8) more physical, temperature dependent ultimate tensile strength is incorporated to estimate the maximum back stress as $\sigma_{max} = 1.5 \times \sigma_{UTS\,(T)}$ and the effective stress is also incorporated instead of applied stress, in the following form,

$$M_{cg} = \frac{D_0 b}{k_B T}\, e^{\frac{\sigma_{eff} b^3}{k_B T}}\, e^{-\frac{Q}{RT}\left[1-\left(\frac{\sigma_{eff}}{\sigma_{max}}\right)^2\right]}. \tag{6.9}$$

6.3.4. Damage

Creep exposure leads to the degradation in the high temperature mechanical properties of materials, thus the components exposed to such conditions fail after some time. Under the creep exposure, most probable strength deterioration mechanisms are the coarsening of precipitates and creep cavity formation. In first case, the precipitate coarsens by decreasing the number density of precipitates in system. The rate at which precipitates coarsen can be derived by differentiating the Ostwald ripening equation $r_{pi}^n - r_{i0}^n = k_{d_i} t$. This leads to,

$$\dot{r}_{p_i} = \frac{k_{d_i}}{n.r_{p_i}^{(n-1)}} \tag{6.10}$$

In the framework of CDM approach and as the function of initial precipitate radius r_{pi0}, the damage parameter can be given as [51],

$$D_{(ppt),i} = 1 - \frac{r_{p_{i0}}}{r_{p_i}} \tag{6.11}$$

If we arrange the Ostwald ripening equation,

$$\left(\frac{r_{p_i}}{r_{p_{i0}}}\right)^n = \frac{k_{d_i} t}{{r_{p_{i0}}}^n} + 1 \tag{6.12}$$

Now, from Equation (6.11) and (6.12), we get,

$$\left(1 - D_{(ppt),i}\right)^{-n} = \frac{k_{d_i} t}{{r_{p_{i0}}}^n} + 1 \tag{6.13}$$

Furthermore, after differentiating Equations (6.13), it follows,

$$\dot{D}_{(ppt),i} = \frac{k_{d_i}}{n\,{r_{p_{i0}}}^n}\left(1 - D_{(ppt),i}\right)^{n+1} \tag{6.14}$$

Therefore, the rate at which damage progresses follows as,

$$\dot{D}_{(ppt),i} = \frac{k_{pi}}{n}\left(1 - D_{(ppt),i}\right)^{n+1},\ where\ k_{pi} = \frac{k_{d_i}}{{r_{p_{i0}}}^n} \tag{6.15}$$

where, k_{di} is the Ostwald coarsening constant, r_{pi} is the radius of i^{th} precipitates and n is a constant related with the coarsening kinetics. In case of $M_{23}C_6$ carbide type of precipitates $n = 3$, and for MX carbonitride type precipitates $n = 5$. Herein, the combined damage that occurs due to the coarsening of both precipitates can be and represented as [55, 58],

$$D_{ppt} = \sum_{i=1}^{2}\left(D_{(ppt),i}\right). \tag{6.16}$$

In second case, creep cavities start to form from the very beginning and their growth and interlinkage leads to the manifestation of micro cracks. These micro cracks eventually lead to failure of the materials. High angle grain boundaries are susceptible to cavity formation and presence of precipitate at these interface makes the material more vulnerable. For such situations, Yin and Faulkner et al. [44] and Surya et al. [57] proposed a model that depends on strain and strain rate both, and cavitation damage rate is expressed as,

$$\dot{D}_{cav} = A\varepsilon\dot{\varepsilon} \tag{6.17}$$

The damage parameter is dimensionless and it lies between zero to one.

6.3.5. Creep strain

Experimentally determined creep strain is resultant of several mechanisms that occurs at different length scale. These mechanisms are; strain accumulation due to movement of dislocations, enhancement of creep strain rate due to damage from the coarsening of different type of precipitates and creep cavitation. The original Orowan equation only considers the strain and strain rate resulted from the dislocation movement, thus, unable to model the tertiary part of creep curves. Invoking the CDM concept, Orowan equation can be modified by considering these additional material softening mechanisms as [58],

$$\dot{\varepsilon} = \frac{b\rho_m v_{cg}}{M(1-D_{ppt})(1-D_{cav})} \ . \tag{6.18}$$

6.4. Results and discussion

6.4.1. Creep curves

Theoretical creep curves were obtained through the current model by solving the modified Orowan Equation (6.18) and governing Equations (6.1) - (6.5), (6.7) and (6.9) - (6.17). The obtained creep curves after simulation are plotted with experimental ones in Figures. 6.2a and b. It is evident that the experimental and simulated creep curves are comparable with good agreement. It can also be observed that material exposed at higher stress at the fixed temperature failed early as compared with lower stress.

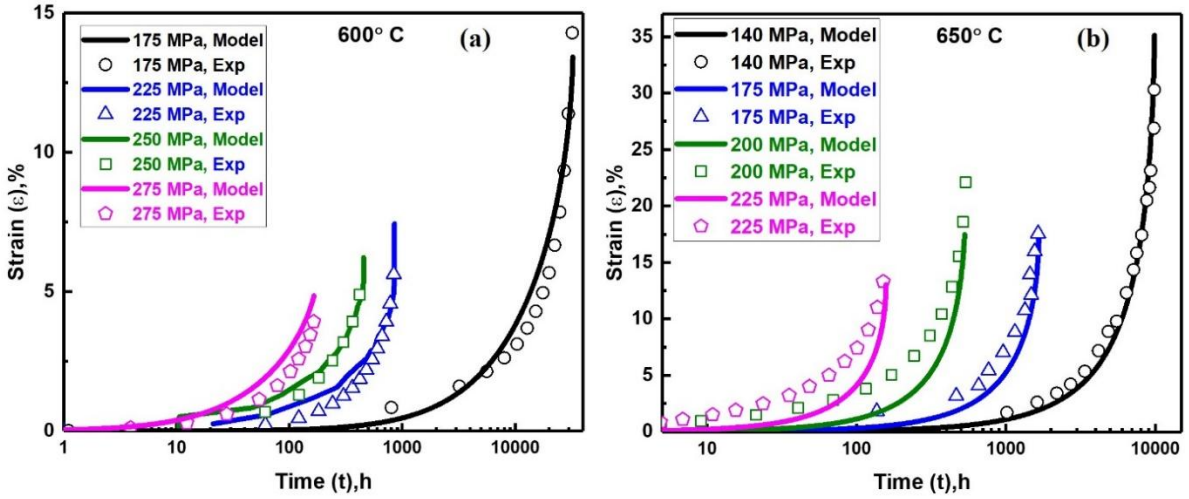

Figure 6.2. Experimental and modelled creep curves of steel 316 LN; (a) Black solid line and circle: 175 MPa, blue triangle and solid line: 225 MPa, green square and solid line: 250MPa Magenta pentagon and solid line: 275 MPa at 600 ^{o}C and (b) Black solid line and circle: 140 MPa, Blue triangle and solid line: 175 MPa, Green square and solid line: 200MPa, Magenta pentagon and solid line: 225 MPa at 650 ^{o}C.

6.4.2. Microstructure evolution

Figures. 6.3a and b depict the variation in ρ_m and ρ_f with exposure time, at the varying creep conditions. The magnitude of both parameters increases with ongoing creep. Steel 316LN is a low stacking fault energy material, having tendency to hardened with creep. Thus, ρ_m and ρ_f increase due to production of new dislocations via Frank-Read (F-R) mechanism. Furthermore, it can be observed through Figures. 6.3a and b that, the dislocation densities have higher magnitude at elevated stresses. The reason is, as the operation frequency of F-R sources can be altered by the application of stresses, higher stress leads to higher operation frequency, hence more production of dislocations. Herein, the magnitude of the ρ_m and ρ_f lies in the range of 7.74×10^{12} - 11.58×10^{12} m^{-2} and 2.27×10^{13} - 3.96×10^{13} m^{-2}, respectively, for the explored conditions. The predicted magnitude can be supported by many available experimental observations in the literature. In a

similar work, ρ_f was observed to have a magnitude of ~ 4.04×10^{13} m^{-2} at 650 ^oC/140 MPa [18]. Mathew et al. [150] reported the ρ to be ~ 1.90×10^{13} m^{-2} at 850 ^oC / 215 MPa for a variant of 316 steel. Christopher et al. [16] reported the ρ_m and ρ_f between ~1×10^{13} - 7×10^{13} m^{-2} and ~1×10^{14} - 1×10^{15} m^{-2}, respectively, at 27-700 ^oC. The above discussion suggests that the predicted values of ρ_m and ρ_f are comparable with [18, 150] reported data (see Table 6.2). It can also be observed that forest dislocation density does not saturates as faster as the mobile one. The mobile dislocations are free to glide easily and act as quick response internal variable. It is known that mobile dislocations after travelling an average glide distance, transform and get forested. However, forest dislocations attain metastable configuration with slow rate, therefore, it takes relatively more time to achieve the saturation values of forest dislocation density [16, 41]. The aforementioned increase in dislocation density predictions is also supported by TEM investigation and micrograph of specimen crept at 650 ^{o} C / 140 MPa is shown in Figure. 6.4. Entangled dislocations with high density (compared to as received) and carbide precipitates can be observed after creep.

Figures. 6.3c and d depict the average dislocation glide distance at the varying creep conditions. Decreases in the average dislocation glide distance followed by the plateau regime can be observed with the exposure time. Average dislocation glide distance heavily depends on dislocation density and it has inverse relation [253, 256]. Furthermore, the influence of stress at constant temperature on the mean free path can also be observed through the Figures. 6.4c and 6.4d. At the higher stress level, the more production of dislocations leads to reduction in average dislocation glide distance. It was observed to be in the range of 9.01-9.50 µm for the investigated cases. Christopher et al. [16] reported the average dislocation glide distance to be in the range of 20-51 µm for 250- 777 ^oC / 3.16×10^{-5} s^{-1} - 3.16×10^{-2} s^{-1}. In case of tensile deformation of 304 HCu stainless steel, Yadav et al. [41] predicted the average dislocation glide distance to be 2-5 µm at 550-700 ^{o} C. Predicted

values and reported data in the literature suggests that average dislocation glide distance is much dependent on the material and the different deformation conditions (see Table 6.3).

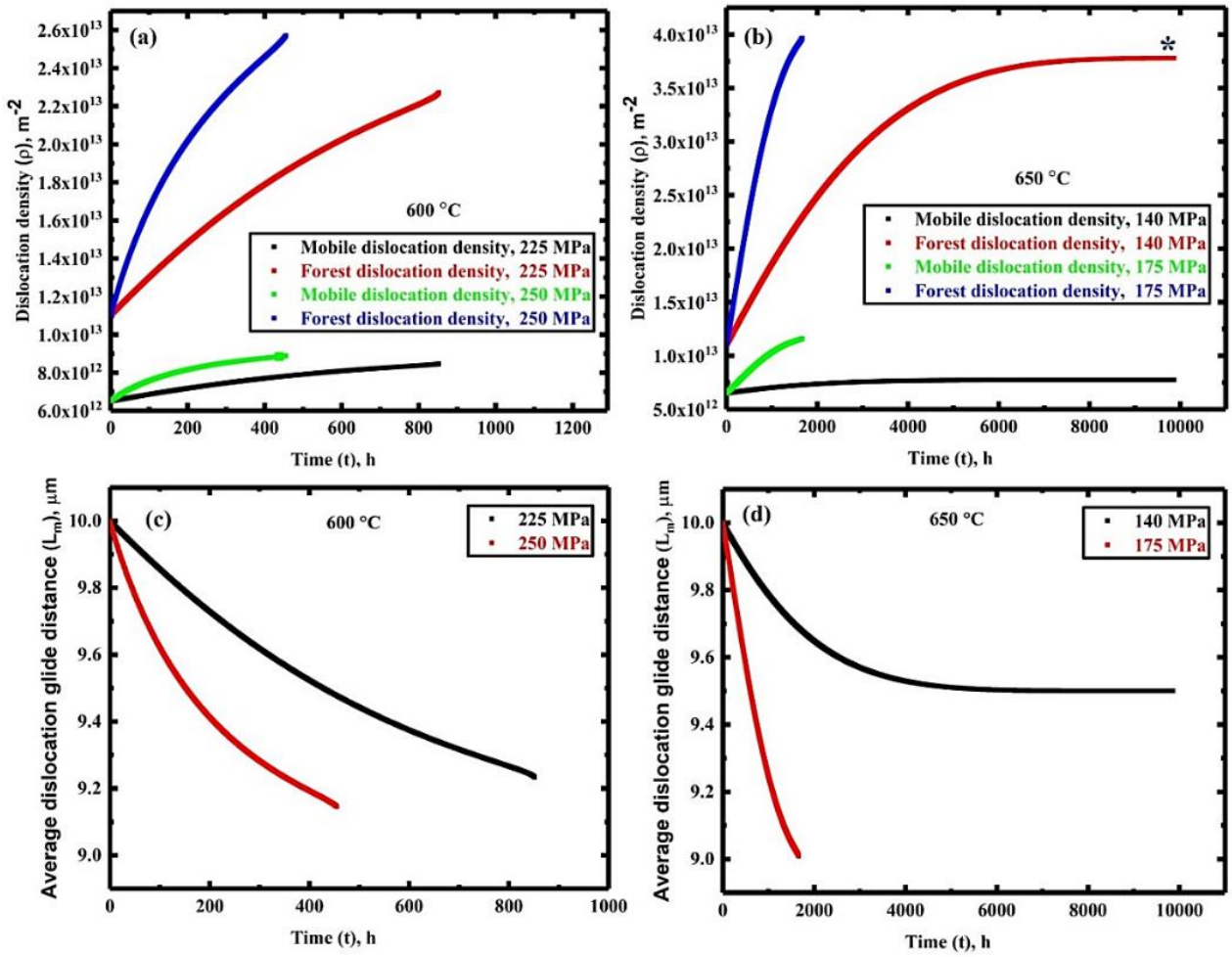

Figure 6.3. Influence of σ_{appl} on dislocation density; (a) Mobile: black line / 225 MPa, Green line / 250 MPa; Forest: red line / 225 MPa, blue line / 250 MPa at 600 ^{o}C, (b) Mobile: black line / 140 MPa, Green line / 175 MPa; Forest: red line / 140 MPa, blue line / 175 MPa at 650 ^{o}C and mean free path: (c) black line / 225 MPa, red line / 250 MPa at 600 ^{o}C, (d) black line / 140 MPa, red line / 175 MPa and at 650 ^{o}C. " ✱ " symbol in Figure. 6.3b represents experimental value of forest dislocation density.

Table 6.2. Output of model at the end of simulation

Parameter	Temp, ^{o}C	600		650		Experimental observations
	Stress, MPa	225	250	140	175	
Mobile ⊥ density, m^{-2}		8.46×10^{12}	8.88×10^{12}	7.74×10^{12}	11.58×10^{12}	$1\text{-}13 \times 10^{13}$ [16, 18, 245]
Forest ⊥ density, m^{-2}		2.27×10^{13}	2.57×10^{13}	3.78×10^{13}	03.96×10^{13}	$10^{14}\text{-}10^{15}$ [16, 18]
Average dislocation glide distance, m		9.23×10^{-6}	9.05×10^{-6}	9.50×10^{-6}	09.01×10^{-6}	$2\text{-}5 \times 10^{-6}$ [41]

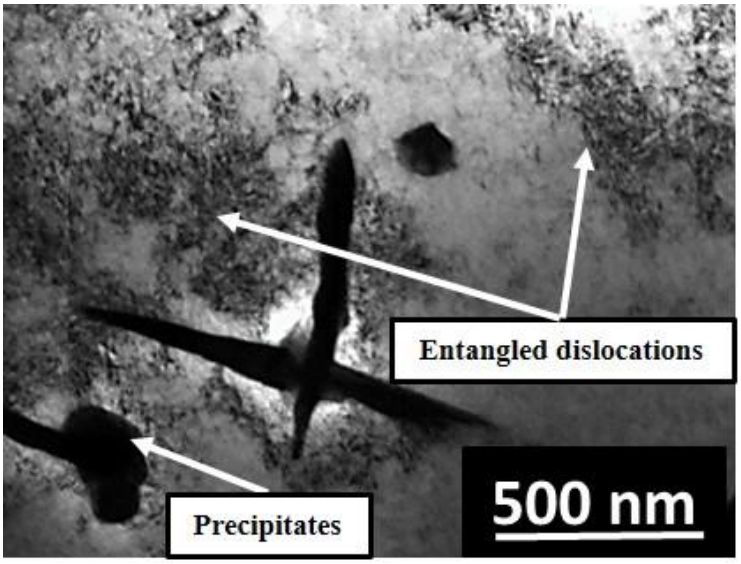

Figure 6.4.TEM micrograph of 316 LN steel (a) 650 ^{o}C / 140 MPa

Figures. 6.5a and b represent the radius of $M_{23}C_6$ carbides and Figures. 6.5c and d represent the radius of MX carbonitrides with the creep exposure time. The radii of the both precipitates are increasing with ongoing creep. Ostwald ripening is the main coarsening mechanism; larger precipitates grows at the expense smaller precipitates. It occurs in order to minimize the surface area per unit volume and surface energy of the system. The radius of $M_{23}C_6$ carbides and MX carbonitrides were observed in the range of 20.37-29.11 nm and 23.74-32.49 nm, respectively for the explored conditions.

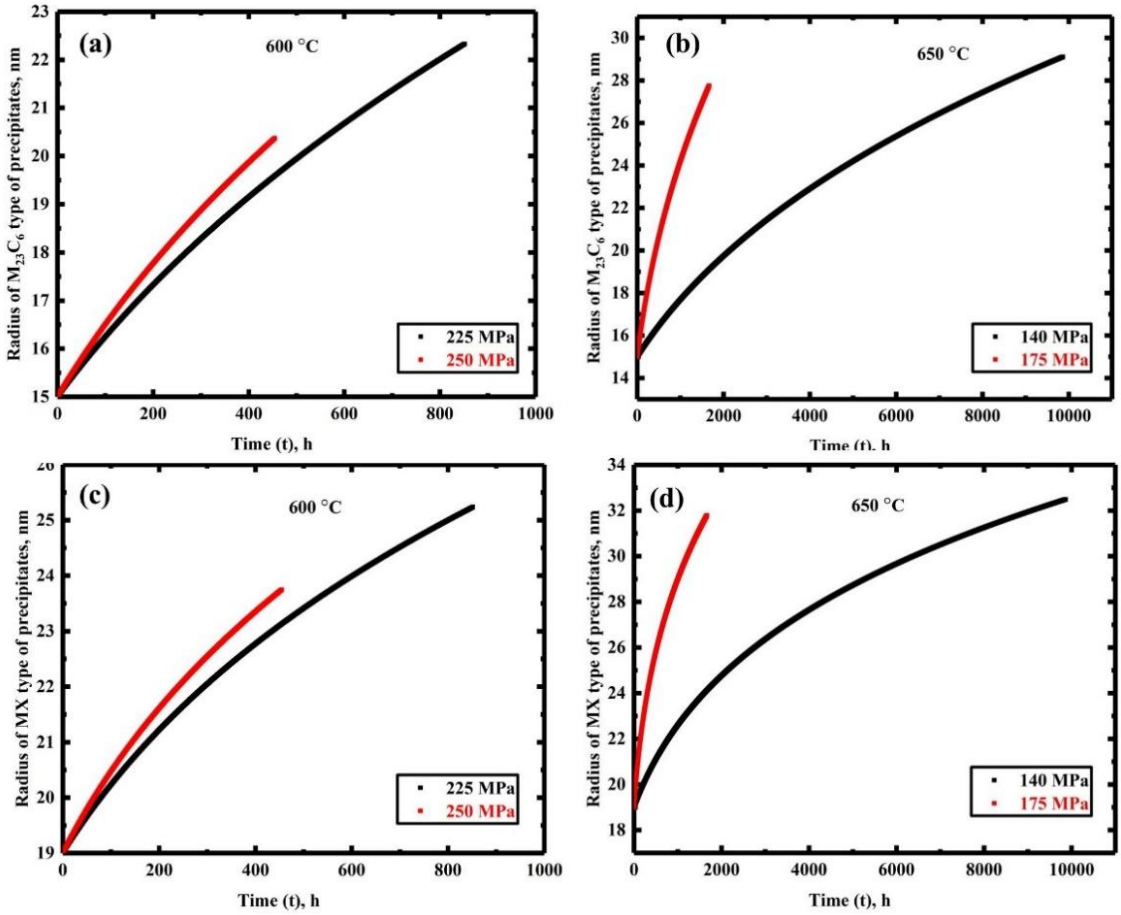

Figure 6.5. Influence of σ_{appl} on radius of precipitates, (a) $M_{23}C_6$-type: black line / 225 MPa, red line / 250 MPa at 600 ^{o}C, (b) $M_{23}C_6$-type: black line / 140 MPa, red line / 175 MPa at 650 ^{o}C, (c) MX-type: black line / 225 MPa, red line / 250 MPa at 600 ^{o}C, (d) MX-type: black line / 140 MPa, red line / 175 MPa at 650 ^{o}C.

6.4.3. Internal stress, effective stress, dislocation velocity, and dislocation mobility

The internal stresses under the various creep tests are shown in Figures. 6.6a and b. As it is directly related to the evolution of dislocation density, it goes up with exposure time and reaches saturation. Since applied stress and dislocation density are closely correlated, it can also be seen that internal stress is larger in magnitude for higher applied stress. The reason is, at higher stresses, dislocation generation increases. It was observed in the range of 68.48-92.02 MPa for the investigated creep

conditions. Similarly, effective stress is shown for various creep tests in Figures. 6.6c and d. Due to the fact that effective stress is defined as the difference between applied and internal stress, it diminishes and saturates with time. Furthermore, as the effective stress is a directly related with the applied stress, it is high for higher applied stress. It was observed between 57.06 - 164.92 MPa in this work.

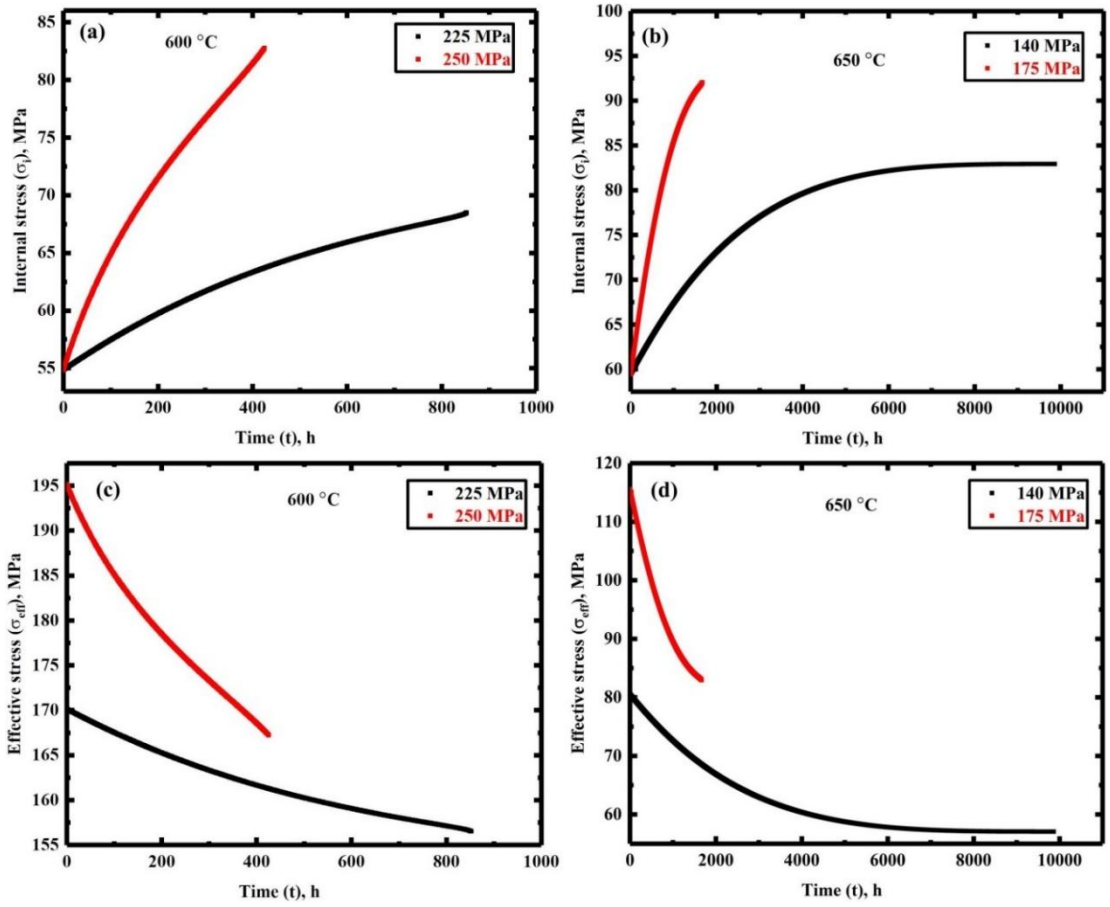

Figure 6.6. Influence of σ_{appl} on internal stress; (a) black line / 225 MPa, red line / 250 MPa at 600 ^{o}C, (b) black line / 140 MPa, red line / 175 MPa at 650 ^{o}C and effective stress; (c) black line / 225 MPa, red line / 250 MPa, at 600 ^{o}C, (d) black line / 140 MPa, red line / 175 MPa at 650 ^{o}C.

For various temperature and stress conditions, the dislocation velocity is shown in Figures. 6.7a and b. Due to the fact that it is directly connected to effective stress, its magnitude is observed to

be decreasing with continued creep. As a result of its association with high dislocation mobility and high effective stress at higher applied stress, it is also possible to conclude that the dislocation velocity is high for the larger magnitude of applied stress. The magnitude of the dislocation velocity was observed to be ranging from 2.37 $\times 10^{-12}$ m/s to 1.45 $\times 10^{-11}$ m/s for the investigated creep conditions.

The dislocation mobility under various temperature and stress conditions is shown in Figures. 6.7c and d. With continued creep, the evolution trend is towards declining until it reaches saturation. A decrease in the dislocation mobility is caused due to the enhanced dislocation population during creep, because they act as obstacles against each other. It was observed that dislocation mobility is high for the higher applied stress.

Table 6.3. Microstructural parameters reported in literature for Fe based alloys

Parameters	**Materials/conditions**	**Magnitude**	**Refs.**
Internal stress	316 LN / 550 ^{o}C / 140 MPa	~ 114 MPa	[18]
Effective stress	550 ^{o}C / 140 MPa	~ 26 MPa	[18]
Dislocation velocity	316 LN / 650 ^{o}C / 120-225 MPa	~5 $\times 10^{-9}$ - 5 $\times 10^{-8}$ m/s	[245]
	Fe15Cr25Ni	~1 $\times 10^{-9}$ – 3.40 $\times 10^{-8}$ m/s	[45]
	Fe-0.7W for 720 ^{o}C / 3.80 MPa	~3.25 $\times 10^{-8}$ m/s	[257]
	Fe-0.7Mo / 738 ^{o}C / 5.30 MPa	~ 2.3 $\times 10^{-8}$ m/s	[257]
Dislocation mobility	Fe-W alloys / 720 ^{o}C	4.3$\times 10^{-15}$ mPa^{-1}s^{-1}	[257]
	Fe-Mo / 738 ^{o}C	4.3 $\times 10^{-15}$ mPa^{-1}s^{-1}	[257]
	P92 / 600 ^{o}C / 150 MPa	2.5 $\times 10^{-19}$ mPa^{-1}s^{-1}	[197]

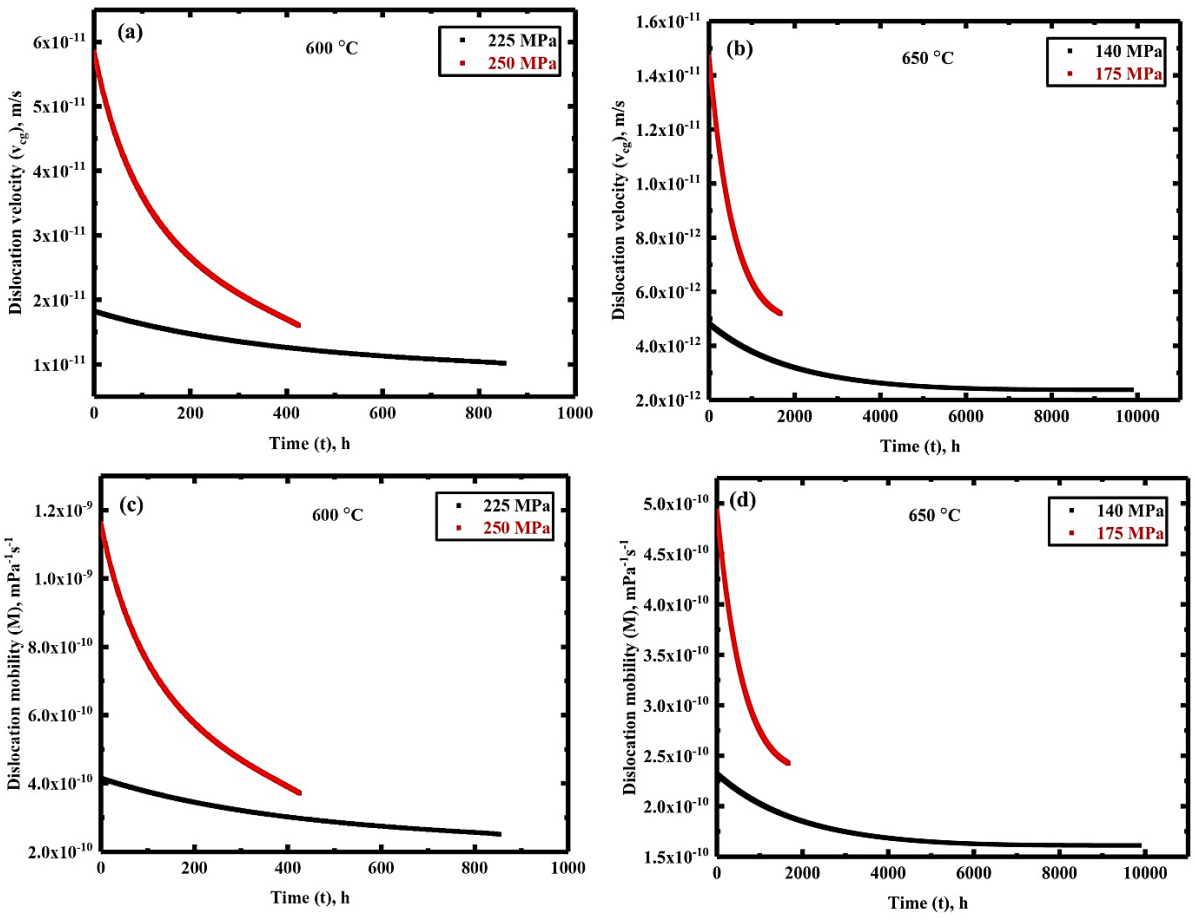

Figure 6.7. Influence of σ_{appl} on dislocation velocity; (a) black line / 225 MPa, red line / 250 MPa at 600 ^{o}C, (b) black line / 140 MPa, red line / 175 MPa at 650 ^{o}C and dislocation mobility; (c) black line / 225 MPa, red line / 250 MPa, at 600 ^{o}C, (d) black line / 140 MPa, red line / 175 MPa at 650 ^{o}C.

Its range was observed to be 1.61 $\times 10^{-10}$ $mPa^{-1}s^{-1}$ to 3.41 $\times 10^{-10}$ $mPa^{-1}s^{-1}$ for the explored creep tests. Mobility data from literature (see Table 6.3) indicates that dislocation mobility greatly depends on the materials and deformation conditions [257].

6.4.4. Damage evolution

The damage progression caused by the coarsening of the two type of precipitates (MX and $M_{23}C_6$) is shown in Figures. 6.8a, b, c, and d. It is apparent that the damage caused by the coarsening of

carbide and carbonitride precipitates is getting worse as the creep continues. The coarsening of the precipitates is attributed to a decrease in energy brought on by a decrease in surface area per unit volume. Additionally, it should be emphasised that with larger applied stress at a certain temperature, second phase particle coarsening occurs quickly. Its known that, high dislocation population at higher stresses serve as both; source and sink for vacancies and conjunction to it an evolved substructure facilitates an easier diffusion path. Additionally, the increased atom jump frequency contributes to the higher coarsening rates at larger stresses. Due to synergistic damage in the local regions, materials loaded at higher stresses fails more quickly than those exposed to lower stresses. Therefore, final size of the precipitates is smaller for higher applied stress than the size of precipitates at the lower applied stress. The damage rate caused by coarsening of carbonitrides precipitate (MX-type) were estimated in this research to be between 1.58×10^{-5} – 3.04×10^{-4} h^{-1}. Similar to this, damage rate caused by the coarsening of carbides precipitate ($M_{23}C_6$-type) ranges from 2.11×10^{-5} to 4.16×10^{-4} h^{-1}. According to Christopher et al. [196] for 9% Cr steel, the total damage rate from all types of precipitates was ~ 2.17×10^{-5} h^{-1} for 600 ^{o}C / 60 MPa. According to Surya et al. [58], for P92 steel, the cumulative damage rate caused by the coarsening of all precipitates ranges between ~ 8.00×10^{-5} to 1.33×10^{-4} h^{-1} for 600 ^{o}C / 145-160 MPa. For grade 91 steel, Surya et al. [57] observed that, for 600 ^{o}C and 80-120 MPa, the total damage rate caused by the precipitate coarsening ranges from ~ 5.26×10^{-6} to 1.11×10^{-5} h^{-1}. From the aforementioned data, it can be said that the damage rate caused by coarsening of precipitates follows the trends from the literature.Cavitation related damage is also shown in Figures. 6.8e and f. As creep strain and strain rate increase, it can be seen that cavitation damage also accelerates. The cavitation phenomenon is significant in steel 316LN because of the presence of carbide type

precipitates at grain boundaries. Cavity development starts when the creep deformation begins, and it gradually grow over time.

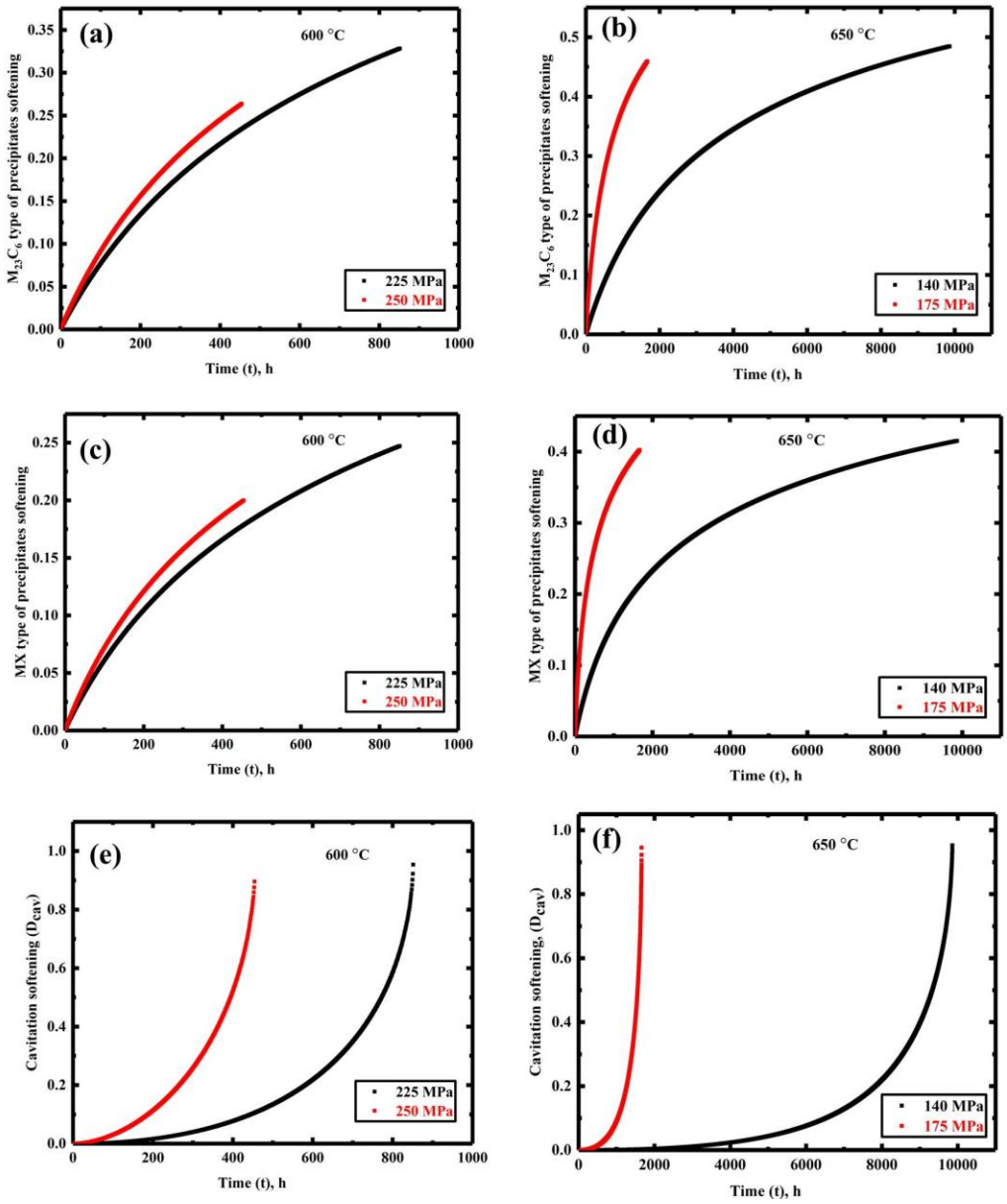

Figure 6.8. Influence of σ_{appl} on precipitate coarsening damage (a) $M_{23}C_6$-type: black line / 225 MPa, red line / 250 at 600 °C, (b) $M_{23}C_6$-type: black line / 140 MPa, red line / 175 at 650 °C, (c) MX-type: black line / 225 MPa, red line / 250 at 600 °C, (d) MX-type: black line / 140 MPa, red line / 175 at 650 °C; (e) Cavitation: black line / 225 MPa, red line / 250 at 600 °C, (d) Cavitation: black line / 140 MPa, red line / 175 at 650 °C

Additionally, it can be shown from the cavitation damage evolution curves that initial damage is minimal. With continued creep, cavities grow more quickly beyond secondary, which causes an increase in damage rate. Finally, in the tertiary regime, cavities start to interlink, which causes a sharp rise in the cavitation damage. The magnitude of the cavitation damage reaches 0.95 more quickly for greater applied stress than at lower applied stress, as shown in Figures. 6.9e and f. When the cavitation damage reaches one, the specimen is believed to be failed. In this study, the cavitation damage rate was increased from 2.88×10^{-4} h^{-1} to 8.17×10^{-4} h^{-1} with increase in stress from 225 MPa to 250 MPa at 600 ^{o}C. Similarly, the cavitation damage rate was increased from 1.43×10^{-5} h^{-1} to 7.88×10^{-5} h^{-1} with increase in stress from 140 MPa to 175 MPa at 650 ^{o}C.

The model predictions are in line with the experimental observations of stress dependent creep cavities and crack formation. Figure. 6.9a depicts the presence of creep cavities developed at the grain boundaries and triple junctions at 650 ^{o}C / 175 MPa. Figure 6.9b shows the more profound damage in terms of cavities transformed to wedge cracks due to higher stress (650 ^{o}C / 200 MPa).

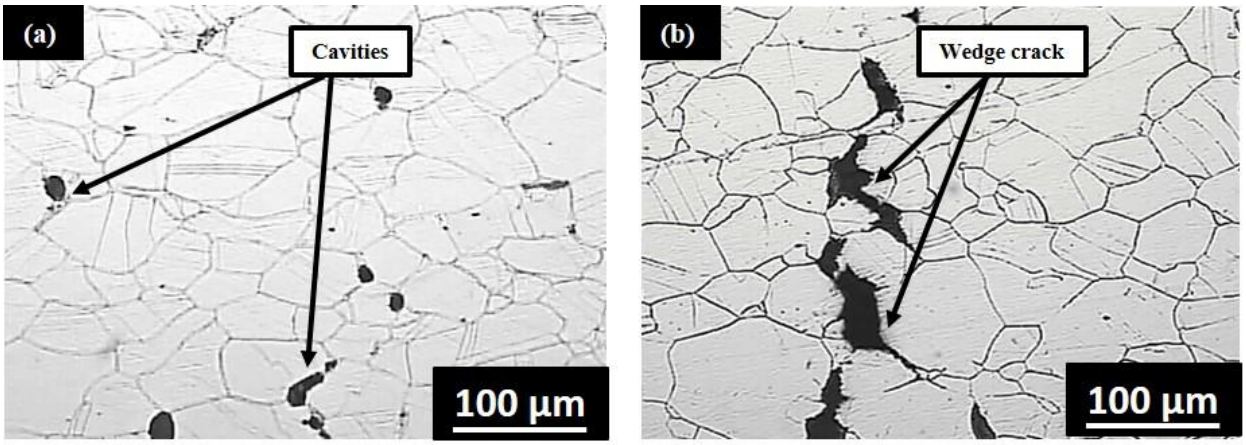

Figure 6.9. Optical micrograph of crept samples at 650 ^{o}C (a)175 MPa, (b) 200 MPa

According to Christopher et al. [199], for 316 L stainless steel, the damage rate ranges from ~ 8.0×10^{-6} h^{-1} to 4.0×10^{-3} h^{-1} at 650 ^{o}C / 110-240 MPa. The cavitation damage rate for P91 steel,

ranges from ~ 1.01×10^{-6} to ~ 2.04×10^{-5} h^{-1} for 600 ^{o}C / 80-120 MPa [57]. It is clear from the discussion above that, the cavitation damage rate follows the trend of the literature [57, 58, 199].

6.4.5. Applicability and usefulness of this model

As pointed out in section 6.3.5, measured creep strain is resultant of three primary factors: dislocation motion, softening due to precipitate coarsening, and softening from creep cavitation. The conventional Orowan equation used in many models [47, 49, 155] addresses the strain accumulation solely from dislocation motion, thus, not able to simulate tertiary creep. Thus, one potential solution to develop two physical models, one for creep strain dealing with dislocation motion (present work) and another addressing the creep cavity formation. These two, creep model and cavitation model needs to be coupled with precipitation kinetics software like MatCalc or Thermocalc. Thus, the cavitation model would update the reduced load-bearing area, while the mean radius and number density of precipitates would be updated at each time step using the precipitation kinetics software. By altering the chemical composition and heat treatments within the software, the initial and evolving precipitation state could be addressed. This would enable the estimation of creep strain for new alloy compositions, facilitating the development of new materials. However, coupling the cavitation model, precipitation kinetics software, and the creep model is highly complex, requiring significant computational power and a multiscale modeling approach.

While addressing the only creep curve predictions, another way is combining physical creep models with continuum damage mechanics (CDM) approach to modify the Orowan equation (see Equation. 6.18). This modification allows the calculation of creep strain that accounts for all three contributing factors-dislocation motion, precipitate coarsening, and cavitation softening. This

approach is simpler and less cost and less time-consuming. Additionally, the evolution of dislocation densities, softening parameters, and other variables responsible for material failure are predicted with ongoing creep time.

The model results delineate that, under the action of stress, dislocation density increases (see Figures. 6.4a and b) while both dislocation velocity (see Figures. 6.7a and b) and dislocation mobility (see Figures. 6.7c and d) decrease for steel 316LN with ongoing creep time. In addition to this, the coarsening of carbide precipitates contributes to a reduction in the material's creep resistance. Higher stresses generate more dislocations, thus, increasing the possibility of dislocation pile-ups at coarse precipitates near grain boundaries, which in turn promotes the formation of creep cavities. Dislocation pile-ups at second-phase particles, combined with precipitate coarsening, appear to be the primary material degradation mechanism, leading to grain boundary cavitation. This explains the early failure of highly stressed samples with relatively short rupture times. While the model performs well for 316LN and outputs are more realistic, it is important to note that it is based on physical parameters that must be carefully optimized when applied to other materials.

This physics-based model offers valuable microstructural insights that can aid in component design and remaining life assessment by providing a more detailed understanding of the complete creep curves. From a practical perspective, this work is highly significant for understanding the microstructural evolution of components like the inner vessel and intermediate heat exchanger that often fail due to creep.

6.5. Summary and Conclusions

Presented hybrid model is capable to address the creep behaviour up to the large portion of tertiary creep regime in 316 LN. Model can deliver creep curves and microstructure evolution together.

The variation of variables that are dislocation densities, average dislocation glide distance, mobility and velocity of dislocations, coarsening of precipitates and respective damage, and damage due to cavitation during creep can be obtained. Hence, this approach is not only for merely curve fitting, rather microstructure reliant parameters can be tracked at every single time step. Outcome of this work is delineated in brief as,

- The mobile dislocations act as quick response internal variable thus saturates at relatively shorter creep time. The forest dislocations are produced once the mobile dislocations get forested. Therefore, forest dislocations attain metastable configuration with slow rate, therefore, it takes relatively more time to achieve the saturation values.
- ρ_m and ρ_f increase and average dislocation glide distance decreases with ongoing creep. Predicted ρ_m, ρ_f and average dislocation glide distance was observed in the range of 7.74 $\times 10^{12}$ - 11.58 $\times 10^{12}$ m^{-2}, 2.27 $\times 10^{13}$ - 3.96 $\times 10^{13}$ m^{-2} and 9.01-9.50 µm, respectively.
- The Internal stress is found to be increasing whereas the effective stress decreasing with ongoing creep. They lie in the range of 68.48-92.02 MPa and 57.06-164.92 MPa, respectively.
- The velocity and mobility of dislocations decrease with accumulated strain. They were observed between 2.37 $\times 10^{-12}$ - 1.45 $\times 10^{-11}$ m/s and 1.61 $\times 10^{-10}$ - 3.41 $\times 10^{-10}$ $mPa^{-1}s^{-1}$, respectively.
- The radius of $M_{23}C_6$ carbides and MX carbonitrides were observed in the range of 20.37-29.11 nm and 23.74-32.49 nm.
- The damage rate caused by the carbonitrides precipitate (MX-type) and carbides precipitate ($M_{23}C_6$-type) are observed between 1.58 × 10^{-5} – 3.04 × 10^{-4} h^{-1} and 2.11 × 10^{-5} – 4.16 × 10^{-4} h^{-1}, respectively.

- Cavitation damage rate was estimated to be between 1.43×10^{-5} h^{-1} and 8.16×10^{-4} h^{-1} for the conditions examined.
- During creep, as more dislocations are produced at higher stresses, the possibility of dislocation pile-ups at coarse precipitates near grain boundaries also increases, which in turn promotes the formation of creep cavities and early failure of specimens exposed to higher stresses.

Appendix 6.A

Table 6.4. Material constants for 316 LN

Constants	Values	Refs.
G (MPa)	$(3\times10^{-7}\ T^4 - 7\times10^{-4}\ T^3 + 0.7643\ T^2 - 358.7700\ T + 135402)$	[41]
M	3.0	[41]
k_B (J/K)	1.38×10^{-23}	
Q (kJ/mol)	280	[106]
UTS (MPa)	-1.1241 T + 1411.8000	[258]
c_f	0.30	[58]
b (m)	2.58×10^{-10}	[41]

Table 6.5 Parameters for the creep simulation of 316 LN

Parameters	600 °C	650 °C	Literature data
	175-275 MPa	140-225 MPa	
$K_{d1,}$ $M_{23}C_6$	8×10^{-33}-5×10^{-30}	6.00×10^{-31}-11×10^{-29}	2×10^{-42} [52]
$K_{d2,}$ MX	7×10^{-48}-5×10^{-45}	9.50×10^{-46}-16×10^{-45}	11×10^{-25} [50]
L_{ms} (m)	8.9×10^{-6}- 9.20×10^{-6}	9.50×10^{-6}-9.05×10^{-6}	0-85×10^{-6} [16]
K_2	1-18	10-15	0.324-500 [16, 27]
K_{Lm}	5-54.5	20-60	0-500 [16]
A	102-550	14.86-120	765-1050 [57, 58]